



# Utilize nano-scale metrology techniques to investigate mechanical, structural, and chemical heterogeneity of mixtures contained incineration bottom ash aggregate



Xingyi Zhu, Ying Yuan, Lihan Li, Dong Liu, Jianming Ling\*

Key Laboratory of Road and Traffic Engineering of Ministry of Education, Tongji University, Shanghai 200092, PR China

## HIGHLIGHTS

- The heterogeneity of MSWIBA at the nanoscale was discussed.
- A combination method of NI, FESEM, and EDX was developed.
- A statistical method was put forward to quantify the heterogeneous degree.

## ARTICLE INFO

### Article history:

Received 7 June 2016

Received in revised form 19 September 2016

Accepted 6 October 2016

Available online 13 October 2016

### Keywords:

Municipal solid waste incineration bottom ash

Cement mortar

Nanoindentation

Phase mapping

Heterogeneity

## ABSTRACT

The utilization of municipal solid waste (MSW) incineration bottom ash (IBA) in the infrastructure construction is a double-win solution to feed the fueling demand for building stones and binding materials. However, MSWIBA is a so highly heterogeneous and variable material that the macro-scale researched results cannot guarantee its behavior at any moment and under any conditions. Therefore, we should figure out why the heterogeneity will happen and how the heterogeneity affects the mechanical behavior of the mixtures. In this paper, the heterogeneity of mixtures contained IBA was investigated at nano-scale from the point of view of chemistry, microstructure, and micromechanics. Nanoindentation (NI) testing together with the image processing technique and statistical method was performed to evaluate the elastic modulus and creep parameters' variation in the measured regions. The test sample was then studied by FESEM observation to illustrate its disordered microstructure. Finally, elemental and phase investigation of the NI sample was carried out by Energy-dispersive X-ray (EDX), which further gave the fundamental arguments why the MSW IBA mixtures present apparent heterogeneous behavior. It can be concluded that nanoindentation elastic/creep testing, FESEM observation, and EDX chemical analysis give mutual verification to illustrate the heterogeneous phenomenon in IBA cement mixtures.

© 2016 Elsevier Ltd. All rights reserved.

## 1. Introduction

Municipal solid waste (MSW) is one of the heaviest and most voluminous wastes generated in worldwide. A new report from the World Bank's Urban Development department estimates the amount of municipal solid waste will rise from the current 1.3 billion tonnes per year to 2.2 billion tonnes per year by 2025. At present, incineration has become a most effective solution for treating MSW. The first China incinerator was built in 1988 in Shenzhen, nowadays the large incineration plants have been extended to more than 200 in China. Incineration bottom ash (IBA) is the most abundant output from the municipal solid waste incineration (MSWI) residues, approximately one ton of waste can produces

200 kg bottom ashes [1–4]. IBA is a coarser or sand or clay in appearance, with a diameter varying between 0.1 mm and 100 mm. Traditional treatment of IBA is sanitary landfilled, may cause waste of land resources and environmental pollution. In the other hand, world's massive infrastructure construction is still in continued boom, greatly fueling demand for building stones and other binding materials. Therefore, the potential utilization of MSW IBA in the infrastructure construction is a double-win solution. For example, it probably can be used as substitute for aggregate, filler, or even cement in road construction, cement concrete structure, embankments or marine applications.

Utilization of incinerator bottom ash in engineering applications has already been researched for many years [5–10]. Abdulahi [11] used IBA as a natural aggregate replacement in an unbound road sub-grade, while Maria et al. [12] used it in a road sub-base. Based on physical, mechanical, and chemical tests, they all believed

\* Corresponding author.

E-mail address: [jmling@tongji.edu.cn](mailto:jmling@tongji.edu.cn) (J.M. Ling).

that IBA is a highly compactable material that can be adopted in paving applications, meanwhile no imply is found resulting in the negative environmental impact. Eymael et al. [13] reported that IBA can be used in asphalt mixtures as a partial replacement of natural aggregates in amounts of up to 25%, however, higher asphalt content is needed because of its porosity. Andrade et al. [7] evaluated the bottom ash used as a substitute for natural sand in concrete. From the compressive strength test results, it showed that the bottom ash concrete gave a satisfactory result with mixtures containing a maximum of 50%. Lee and Li [14] observed that the major constituents of IBA are similar to those of cement raw materials, when the ordinary cement was replaced by incinerator bottom ash partially, the lower flow values and higher shrinkage can be found, and however, the compressive strength will be highly enhanced. Kim et al. [15] thought that because of the pozzolanic activity in bottom ash, the particle bonding effect is enhanced, resulting in the increase of shear strength and stiffness of mixtures. Therefore, they mixed the IBA with marine dredged soil deposits and cement to upgrade the strength of bottom ash-added composite geomaterial [16].

Above literatures indicate that the use of MSW IBA in infrastructure construction is feasible from the point of view of both structural properties and environment safety. However, Forteza et al. [17] pointed out that MSW IBA is a so highly heterogeneous and variable material that the researched results cannot guarantee its behavior at any moment and under any conditions. A series of reports based on the physical and mechanical tests proved above statement [18,19,2,20]. For example, an unconfined uniaxial compression test of bottom ash materials was conducted by Chimenos et al. [21], they found out that the different specimens tested for a given curing time present a wide range of variation of both unconfined compressive strength and modulus of elasticity, see Fig. 1. Even for the parallel tests, a great difference between the lowest value and the highest value cannot be neglected, leading to a high variance. The key problem is that failure in the disordered materials always involves the progressive local concentrations of tensile stress [22]. Then, under that tensile stress, the micro-cracks are initiated and propagated at the stress concentrated area, finally resulting in the structure failure. Actually, the exact failure mode is highly dependent on the inhomogeneity of materials and the heterogeneity of microstructures [23–25]. Unfortunately, under most situation, inherent heterogeneity is rather complicated and uncertainty. Therefore, for most disordered materials, it is hardly possible to predict physical and mechanical phenomenon of damage processes accurately at structural scale.

Small-scale heterogeneity can always explain experimental variability and non-linearity. Since mixtures containing bottom

ash aggregates are a class of complex chemo-mechanical materials that possess a high degree of heterogeneity from atomistic scales to the macroscopic scales, nano-scale metrology techniques can be adopted to establish the link among chemical-composition, microstructure, and micromechanical performance of bottom ash mixtures, which can be further used as evidences to illustrate why the heterogeneity will happen and how the heterogeneity affect the mechanical behavior of the mixtures. If we grasp these rules, then materials selection criteria and micro-structure combination schemes are ready to be put forward.

Nanometrology is concerned with the science of measurement at the nanoscale level. Some of the popular ones are Scanning Electron Microscopy (SEM) and Field Emission Scanning Electron Microscopy (FESEM) for morphology observations, X-ray Diffraction (XRD) and Energy Dispersive Spectrometer (EDS) for elemental analysis, and Nano-indentation (NI) and Atomic Force Microscopy (AFM) for mechanical test. Nanometrology techniques have been successfully implemented in civil engineering applications, such as the rejuvenating effect on asphalt binders [26], interfacial transition zone properties of recycled aggregate [27], viscoelastic behavior of time-dependent material [28], phase-to-mechanical property of cement-based materials [29], interface adhesion of multilayered films [30], etc.

The objective of this paper is to investigate the heterogeneity of mixtures contained municipal solid waste incineration bottom ash aggregate from the point of view of chemistry, microstructure, and micromechanics. In this regard, MSW IBA samples were prepared and basic properties at macro-scale, such as gradation, content, morphology, main chemical composition, and physical parameters, were tested. Nanoindentation testing together with the image processing technique and statistical method was performed to evaluate the elastic modulus and creep parameters' variation in the measured regions. The test sample was then studied by FESEM to observe its disordered microstructure. Finally, elemental and phase investigation of the NI sample was carried out by Energy-dispersive X-ray (EDX), which further gave the fundamental arguments why the MSWI BA mixtures present apparent heterogeneous behavior.

## 2. Materials and methods

### 2.1. Specimens preparation

#### 2.1.1. Basic properties of municipal solid waste incineration bottom ash samples

The final solid residues used in the test were collected from a waste incinerator plant in Hangzhou 2014–July, China. Usually,

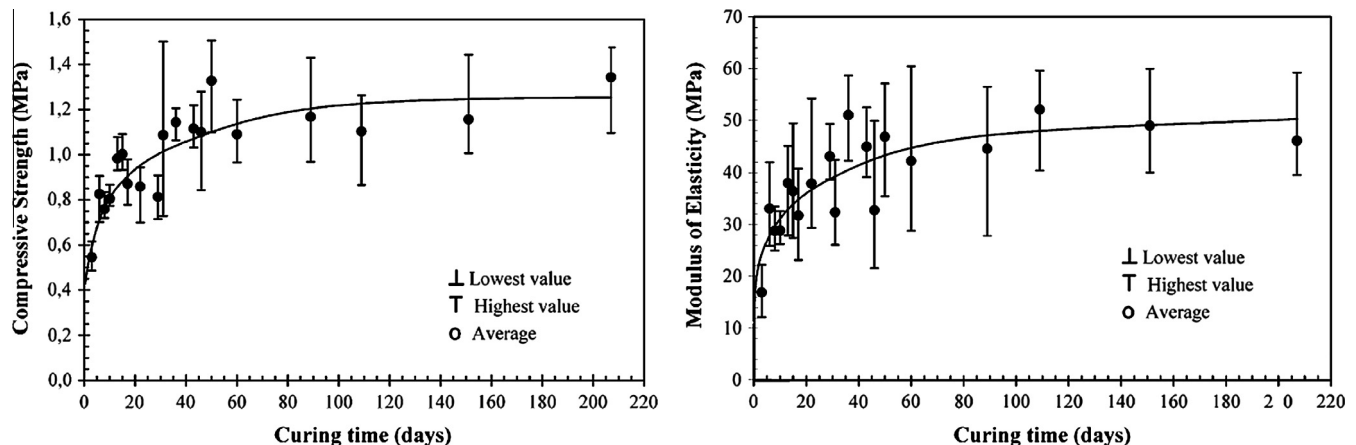


Fig. 1. Compressive strength and modulus of elasticity for IBA varying with curing time [21].

**Table 1**

Gradation of adopted incineration bottom ash.

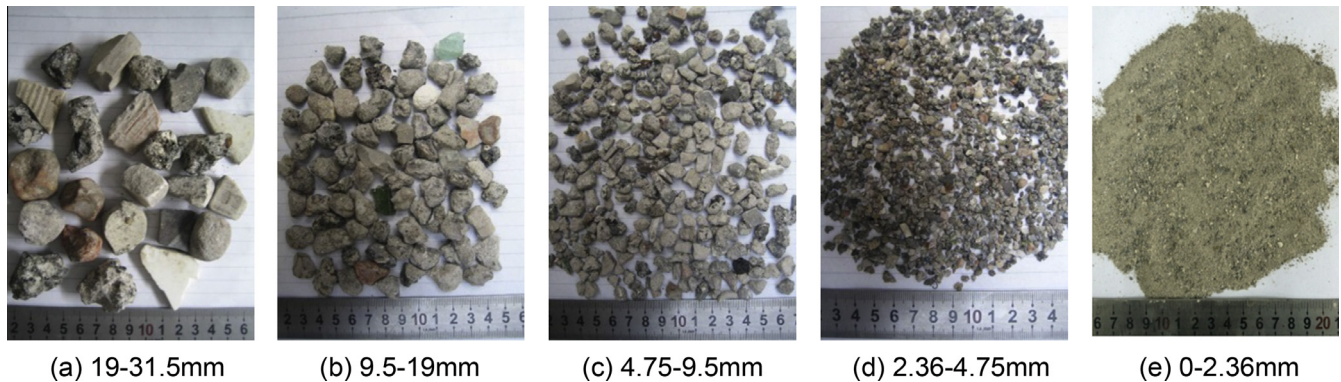
No.	Passing ratio/%												
	Sieve size (mm)												
	31.5	26.5	19	16	13.2	9.5	4.75	2.36	1.18	0.6	0.3	0.15	0.075
1	90.9	87.2	79.0	74.6	66.7	58.6	44.1	34.0	26.9	23.0	15.3	9.1	3.6
2	90.9	90.7	84.6	80.3	74.1	65.1	50.7	40.6	32.3	27.6	18.2	10.1	3.1
3	82.4	80.3	75.2	72.1	67.8	59.7	46.5	36.9	29.2	25.0	16.4	8.3	1.8
Average	88.1	86.1	79.6	75.7	69.5	61.1	47.1	37.2	29.5	25.2	16.6	9.2	2.8

the incineration bottom ashes can be sieved into a well-graded gradation, see Table 1. A small variability of gradation can be found from the same batch. However, the composition of IBA is quite complex and heterogeneous, including glass, brick, ceramics, metal, and slag, see Fig. 2. The content of each component is listed in Table 2. For the smaller sieve sizes (0–2.36, 2.36–4.75), slag is a main output of the incineration by-products. However, there are still 0.3–0.4% impurity substances contained. SEM photographs of slag particles can be found in Fig. 3a. Apparently, it is a very porous and irregular particle. Its porosity may have an influence on the strength, absorption, adhesion, and field compaction behavior of the structure. Besides, residual active chemical substances are usually attached to the surface of the slags. Then, oxidation, carbonation, and hydration reactions can occur when they are exposed in an enough humid environment. For example, flocculent C-S-H gel (Fig. 3(b)), sheet-like  $\text{Ca}(\text{OH})_2$  crystal (Fig. 3(c)), and other amorphous or poor crystallization substances (Fig. 3(e)) can be found in the surface of the slags. All above products make the composition more disordered. For sieve size larger than 26.5 mm, no slags are contained, only ceramics and bricks can be found. Since the strength and the stiffness of ceramics and bricks are rather low, they cannot be used as construction materials. As for the sieve sizes smaller than 19 mm, the component contents are quite differ.

Although slags make up a large majority, the quantity variability of the other four impurity components cannot be neglected, which leading to the difficulty in predicting accurately the mechanical and failure behavior of road structure containing bottom ash.

The chemical composition of incineration bottom ash was measured by X-ray fluorescence spectrometer (BRURER AXS, SRS 3400). As a comparison, the chemical compositions of typical road construction materials, limestone and cement, were also listed in Table 3. Because of the fully oxidation reaction, a large amount of oxides exist in the incineration bottom ash, which account for approximately 84% of the total weight. The proportion of main constituent materials of IBA is quite similar to the cement. Especially, the potentially active oxide, such as  $\text{Al}_2\text{O}_3$  and  $\text{CaO}$  can be found in IBA with a high concentration. However, higher content of heavy metal ( $\text{ZnO}$ ,  $\text{BaO}$ ,  $\text{PbO}$ ,  $\text{Cr}_2\text{O}_3$ ) and salts ( $\text{SO}_3$  and  $\text{Cl}$ ) can be found in the IBA.

Table 4 gives the physical properties of IBA and two kinds of commonly used aggregates (limestone and basalt). The apparent density of IBA is around  $2.1\text{--}2.7\text{ g}\cdot\text{cm}^{-3}$ , much lower than the limestone and basalt, indicating a lighter weight compared to the natural aggregates. Besides, the crushing value and water absorption rate of IBA are much higher than the other two natural aggregates. The main reason is that the high porosity existed in the IBA

**Fig. 2.** Components for different sieve sizes.**Table 2**

Content of each component.

Sieve size/mm	Content/%				
	Metal	Ceramic	Brick	Glass	Slag
>31.5	–	50.0	50.0	–	–
26.5–31.5	–	55.1	44.9	–	–
19–26.5	0.4	46.9	22.9	5.5	24.0
16–19	3.7	25.9	2.9	21.8	44.3
13.2–16	2.3	28.6	16.0	17.5	35.4
9.5–13.2	3.1	12.6	15.9	23.1	43.9
4.75–9.5	2.1	4.6	1.3	13.9	77.7
2.36–4.75	0.4	–	–	–	99.6
0–2.36	0.3	–	–	–	99.7

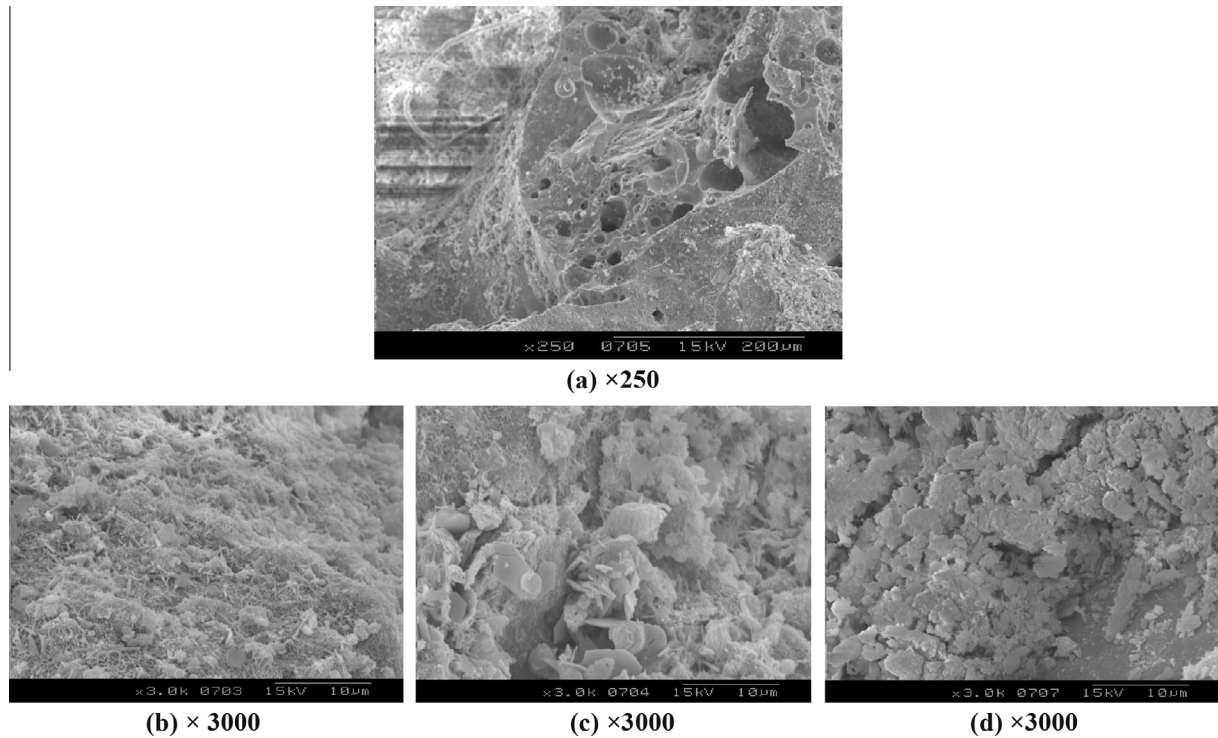


Fig. 3. SEM photographs of the surface of the slag particles.

Table 3

Main chemical composition of adopted incineration bottom ash and typical road construction materials.

Chemical composition	SiO <sub>2</sub>	Al <sub>2</sub> O <sub>3</sub>	CaO	Fe <sub>2</sub> O <sub>3</sub>	MgO	P <sub>2</sub> O <sub>5</sub>	Na <sub>2</sub> O	K <sub>2</sub> O	ZnO	SO <sub>3</sub>	Cl	BaO	PbO	Cr <sub>2</sub> O <sub>3</sub>
IBA	19.40	6.17	39.00	4.27	2.47	5.77	1.69	1.49	0.55	3.02	3.39	0.29	0.06	0.05
Limestone	1.01	0.27	56.27	0.27	0.057									
Cement	32.5	6.23	40.30	3.41	0.82	0.4	0.27	1.07	0.03	1.52	0.2			0.02

Table 4

Physical properties of IBA and natural aggregate.

Aggregate type	Sieve size/mm	Crushing Value/%	Apparent density /(g·cm <sup>-3</sup> )	Water absorption rate/%
IBA	0–2.36		2.667	
	2.36–4.75	30.0	2.410	7.0
	4.75–9.5	38.7	2.198	7.2
Limestone	0–5		2.708	
	5–10	18.7	2.825	1.26
	10–20	28.4	2.739	0.44
Basalt	0–3		2.863	
	3–5	20.8	3.009	2.41
	5–10	21.5	2.998	2.17
	10–15	22.1	2.985	1.70

decreases the strength of IBA aggregate and promotes the rate of water absorption.

To better understand the heterogeneity of IBA itself, the mineral composition of IBA produced in different time at different cities was investigated by X-ray diffractometer (XRD). Fig. 4 shows the XRD patterns for the IBAs produced in May 2012, September 2013, January 2015 at Shanghai, and produced in January 2014, July 2014 at Hangzhou. Note that the sample produced in January 2014 at Hangzhou was treated by shaking table, and the rest samples were treated by eddy current separation method. Different from Table 4 showing the IBAs' chemical compositions, Table 5 illustrates the IBAs' mineral compositions which were obtained from the XRD patterns. In Fig. 4, the shape of diffraction peaks of

all the samples are similar and some peaks appear at the same scan angle (see  $2\theta = 20.8^\circ$ ,  $26.6^\circ$ ,  $36.5^\circ$  and  $2\theta = 23^\circ$ ,  $29.3^\circ$ ,  $35.9^\circ$ ,  $39.3^\circ$ ), which suggests that the five samples had the same primary minerals such as SiO<sub>2</sub>, CaCO<sub>3</sub> (see Table 5). However, the IBA from Shanghai contained mineral compositions such as CaO·SiO<sub>2</sub>, 3CaO·Al<sub>2</sub>O<sub>3</sub>, Ca<sub>4</sub>SiO<sub>6</sub> (CO<sub>3</sub>)(OH)<sub>2</sub>, and Na<sub>2</sub>SO<sub>4</sub> which were not found in the IBA from Hangzhou. The heterogeneity of IBA from different cities may be attributed to the different waste composition. Moreover, even produced at the same city, the mineral composition of IBA was different because of manufacturing date. For example, NaNO<sub>3</sub>, MgCO<sub>3</sub> existed only in the sample SH-May 2012, Ca<sub>4</sub>Al<sub>2</sub>O<sub>6</sub>Cl<sub>2</sub>·10H<sub>2</sub>O was found only in SH-Sep. 2013, and Ca<sub>2</sub>SiO<sub>4</sub>·0.05Ca<sub>3</sub>(PO<sub>4</sub>)<sub>2</sub> was detected only in SH-Jan. 2015. As for the effect of production



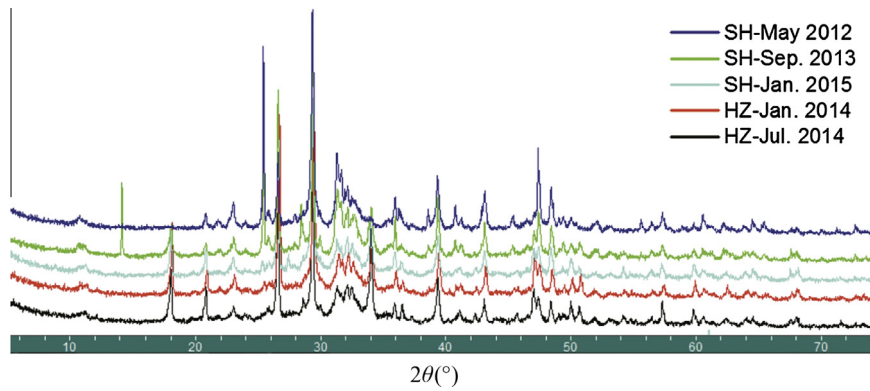


Fig. 4. XRD patterns for the different IBAs.

Table 5

Mineral composition of the different IBAs.

Molecular formula	SH-May 2012	SH-Sep. 2013	SH-Jan. 2015	HZ-Jan. 2014	HZ-Jul. 2014
SiO <sub>2</sub>	✓	✓	✓	✓	✓
CaCO <sub>3</sub>	✓	✓	✓	✓	✓
CaSO <sub>4</sub>			✓	✓	
CaSO <sub>4</sub> ·0.5H <sub>2</sub> O	✓		✓	✓	
CaO·SiO <sub>2</sub>			✓		
3CaO·SiO <sub>2</sub>			✓		
2CaO·SiO <sub>2</sub>	✓	✓	✓		✓
3CaO·Al <sub>2</sub> O <sub>3</sub>			✓		
CaAl <sub>2</sub> SiO <sub>8</sub> ·4H <sub>2</sub> O	✓	✓	✓		✓
Ca <sub>6</sub> (SiO <sub>4</sub> )(Si <sub>2</sub> O <sub>7</sub> )(OH) <sub>2</sub>	✓	✓		✓	
MgCO <sub>3</sub>	✓				
Ca <sub>7</sub> (Si <sub>6</sub> O <sub>18</sub> )(CO <sub>3</sub> ) <sub>2</sub> H <sub>2</sub> O	✓	✓	✓		✓
6CaO·3SiO <sub>2</sub> ·H <sub>2</sub> O	✓	✓			✓
K <sub>2</sub> Ca <sub>5</sub> (SO <sub>4</sub> ) <sub>6</sub> ·H <sub>2</sub> O				✓	
Ca <sub>4</sub> Si <sub>2</sub> O <sub>6</sub> (CO <sub>3</sub> )(OH) <sub>2</sub>		✓	✓		
Ca <sub>2</sub> SiO <sub>4</sub> ·0.05Ca <sub>3</sub> (PO <sub>4</sub> ) <sub>2</sub>			✓		
Ca <sub>4</sub> Al <sub>2</sub> O <sub>6</sub> Cl <sub>2</sub> ·10H <sub>2</sub> O		✓			✓
NaCl	✓			✓	
KCl				✓	
NaNO <sub>3</sub>	✓			✓	
Na <sub>2</sub> SO <sub>4</sub>			✓		

processes, we found that there are several strong diffraction peaks at  $2\theta = 28.3^\circ$ ,  $31.7^\circ$ ,  $40.6^\circ$  in the sample (HZ-Jan. 2014) treated by shaking table, which indicated that KCl exists in the IBA. The heterogeneity of the IBAs could result from the different separation process, particularly treated by shaking table, the wastewater with high chloride ion concentration can promote absorption of chloride ions in IBAs with increasing of immersion time.

Based on the analysis of mineral composition of the different IBAs, it could be concluded that the IBA itself was heterogeneous because of different sources, production data and production processes. Thus attention should be paid on the heterogeneity of IBAs when combined with cement.

### 2.1.2. Nanoindentation samples of IBA blended in cement mortars

The cement mortars contained IBA were mixed to make the nanoindentation sample. The sample preparation procedure can be described as follows. (1) The cementitious materials, IBA with sieve size <9.5 mm, and water were blended together, the bottom ash aggregate/cement/water ratio is 3:1:0.8. (2) A 15 mm × 15 mm × 15 mm cube was trimmed by using a diamond saw. Then, the cement mortar cube was embedded into the bakelite resin which has 30 mm in diameter and 20 mm in height. (3) To guarantee the accuracy of NI test, the sample surface should be smooth enough, therefore, the specimen was grinded on 180, 600, 1200, 2500, 5000 grit abrasive papers one after another. After grinding, the specimen was polished with polishing cloth, see Fig. 5

(a). The specimen was then cleaned with the specimen in alcohol in an ultrasonic bath for 5 min. The whole process took about 2 h until the entire surface has been thoroughly smoothed. As pointed by Miller, after a relatively short polishing duration, 2–4 h, the sample can have a suitably prepared surface which is similar to the results of any longer polishing durations [31].

The final prepared sample for nanoindentation test can be found in Fig. 5(b). A clear image of test area was found, which means the sample has a good surface roughness. Besides, five main components, namely, metal, slag, ceramic, glass, and brick have been contained in the test sample.

### 2.2. Nanoindentation modulus testing

Nanoindentation is a quantitative technique and its basic outputs are elastic modulus and the hardness of the sample. Here, a Hysitron TI 950 Tribo-Indenter was used to measure the mechanical properties of the prepared sample with a cube corner indenter made of diamond. Nanoindentation tests were performed in the load-controlled feedback mode. Normally, the NI instrument can be set into load or depth control mode. The load-controlled mode is more commonly used in the elastic modulus measurement of cementitious material. Moreover, this mode is also quite suitable for creep test, since in the creep test, the maximum load should be held at a fixed value and the change of depth is recorded over a period of time to get the creep behavior of the specimen. The

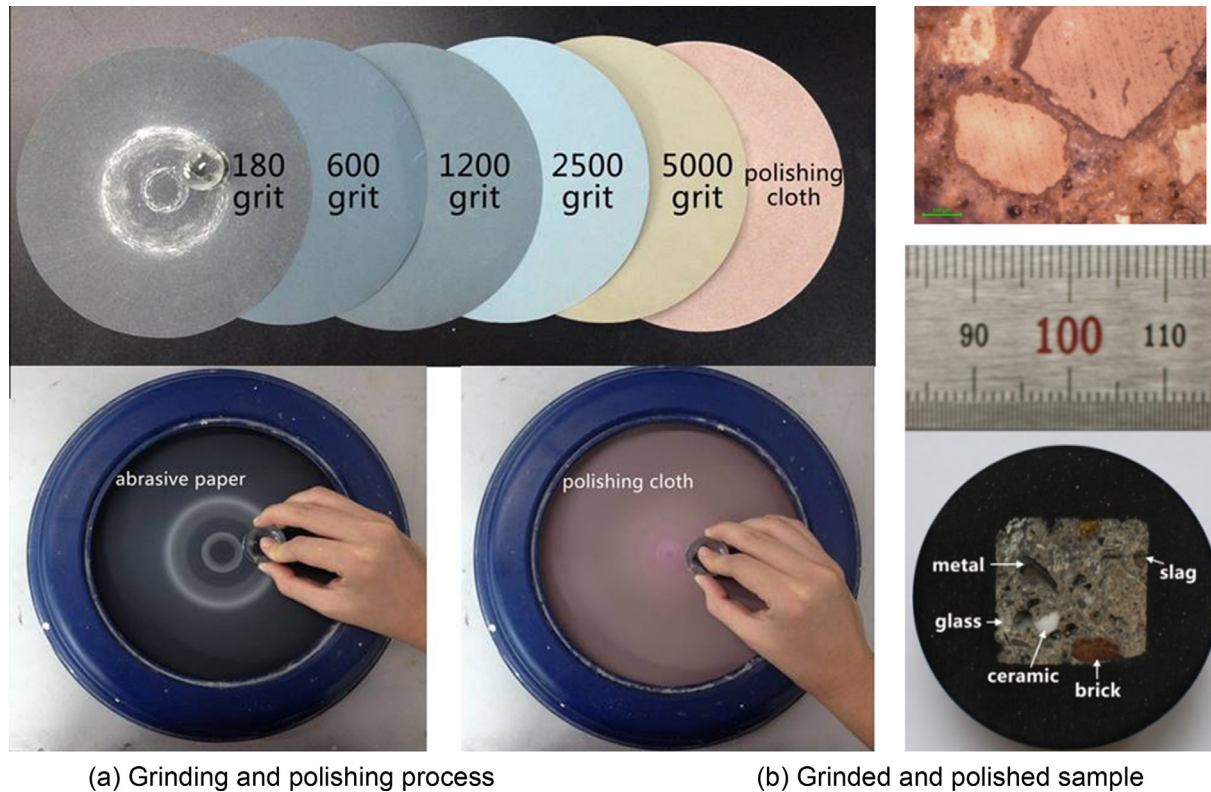


Fig. 5. Nanoindentation sample preparation.

maximum load value in this study was determined according to the arrangement of test points. It is suggested that the distance between two adjacent test points should be larger than the residual imprint produced by maximum load in order to ensure that successive measurements are independent of one another [32–34]. In our paper, a rectangular indentation grid comprised of 231 measurement points was performed on the sample, spaced 5  $\mu\text{m}$  in the X direction and 10  $\mu\text{m}$  in the Y direction. Therefore, the maximum load was set as 1.2 mN in this NI test, whose residual imprint is around 0.8  $\mu\text{m}$ . Meanwhile, the NI test was well carried out in load-controlled mode with a predetermined load (1.2 mN) on cementitious materials containing recycled aggregates, see Refs. [35,36].

The force was applied to drive an indenter probe into the sample surface and the load increased at a constant rate until it reached some peak value, and then decreased the load to zero by withdrawing the probe. The whole applied load ( $P$ )/indenter displacement ( $h$ ) process was continuously monitored see Fig. 6. After that, the elastic modulus of the sample ( $E_s$ ) can be calculated as follows:

$$E_s = (1 - \nu_s^2) \left( \frac{1}{E_r} - \frac{1 - \nu_i^2}{E_i} \right)^{-1} \quad (1)$$

where  $E_r$  and  $E_i$  are the reduced elastic modulus and indenter's elastic modulus, respectively;  $\nu_s$  and  $\nu_i$  are the Poisson's ratio of sample and indenter, respectively. Here,  $E_r$  is defined by the equation

$$E_r = \frac{S\sqrt{\pi}}{2\sqrt{A_c}} \quad (2)$$

in which  $S$  is the initial unloading stiffness, see Fig. 6(c), while  $A_c$  is the projected contact area which should be evaluated at maximum load.  $A_c$  is basically the function of contact depth  $h_c$ , and related to the geometry of the indenter, see as follows:

$$A_c = f(h_c), \quad h_c = h_{\max} - \varepsilon \frac{P_{\max}}{S} \quad (3)$$

where  $\varepsilon$  depends on indenter geometry but usually equals 0.75. Since the maximum depth and the maximum load can be measured, and the initial unloading stiffness can be determined from the collected data, then finally the elastic modulus of the sample can be easily obtained.

In the study of the cement mortar contained IBA, the maximum load was set as 1.2 mN. To ensure a sufficient population of indents to conduct a statistical analysis, a matrix of  $21 \times 11$  indentations with spacing of 5  $\mu\text{m}$  transversely and 10  $\mu\text{m}$  longitudinally was applied to the sample for map investigation with a 100  $\mu\text{m}$  square crossing the chosen region. Here, the chosen region should contain enough information of different components. Based on the Optical Microscope observation, the indented area is determined, in which several typical components can be detected (displayed visually in different color), marked as Zone 1–Zone 6, see Fig. 7.

### 2.3. Time-dependent nanoindentation testing

A less well-known application of nanoindentation is the evaluation of the creep behavior of test samples. Although cement concrete is not a typical viscoelastic material, however, the creep of concrete within the service life is still a distinct and tough problem. In a nanoindentation creep test, an indenter probe was forced into a material surface quickly, and the force was then held constant while the deformation of the material was monitored, see Fig. 8. Here, the maximum holding load was set as 1.2 mN and held for 30 s. The theoretical time-penetration depth curve ( $h_{\max}(t)$ ) of NI tests can be directly derived. To determine the material parameters from the NI creep test data, the time-penetration depth curve should be transferred to the time-creep compliance curve.

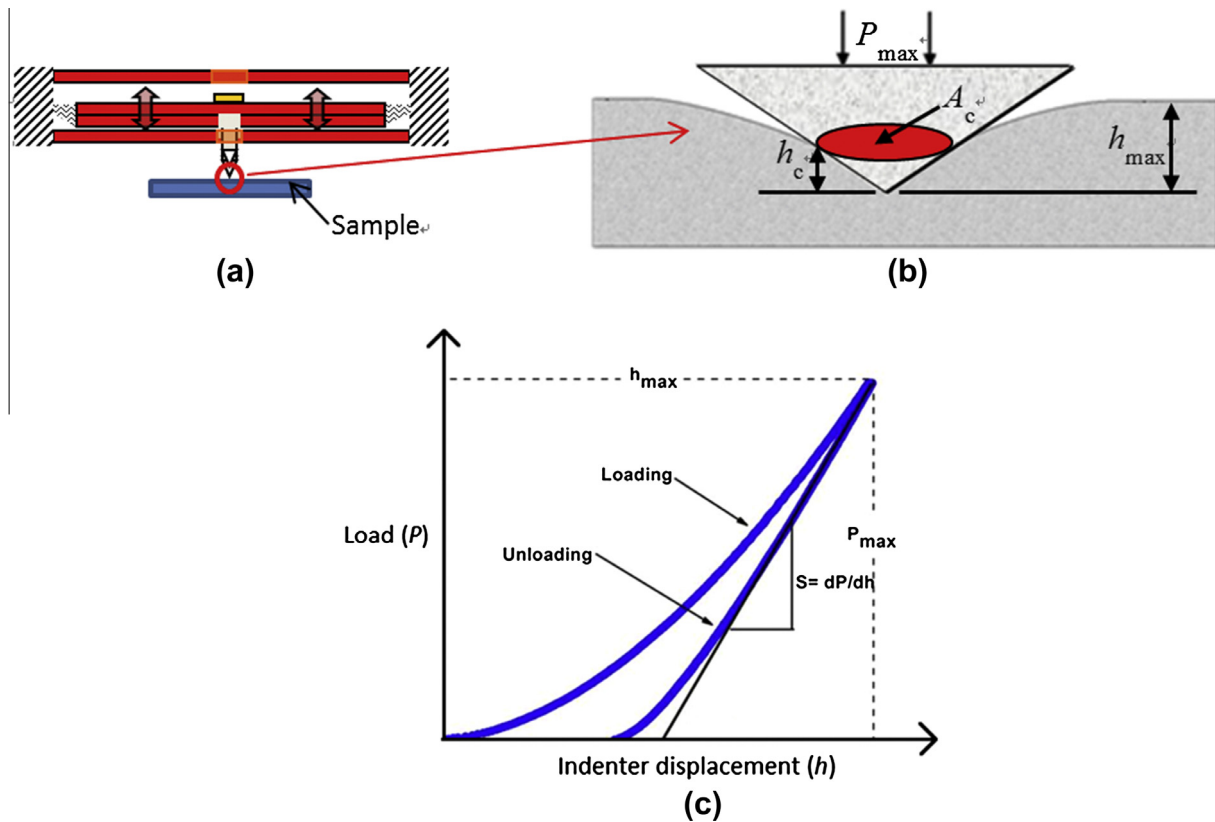


**Fig. 6.** (a) Hysitron three-plate, force-and-displacement sensing transducer; (b) Schematic to illustrate a indenter probe driven into the sample surface; (c) Indentation displacement vs. applied load curves.

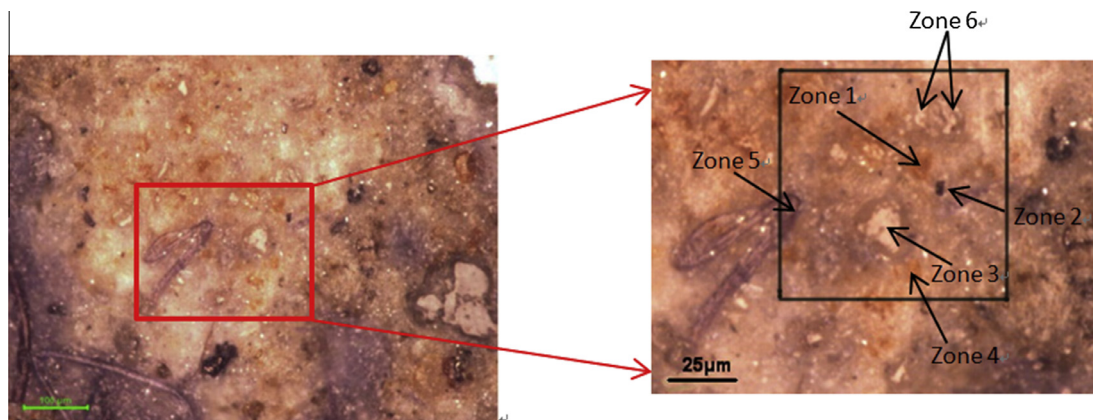


**Fig. 7.** Indented area observed from optical microscope.

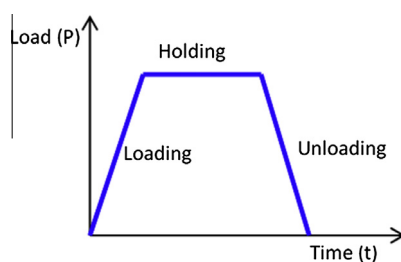


**Fig. 8.** Loading history for nanoindentation creep test.

Typically there are three regions in creep behavior, primary creep, secondary creep, and tertiary creep, see Fig. 9. Primary creep is also called as transient creep, with continuously decreasing creep rate, the slope of the creep curve diminishes with time. For

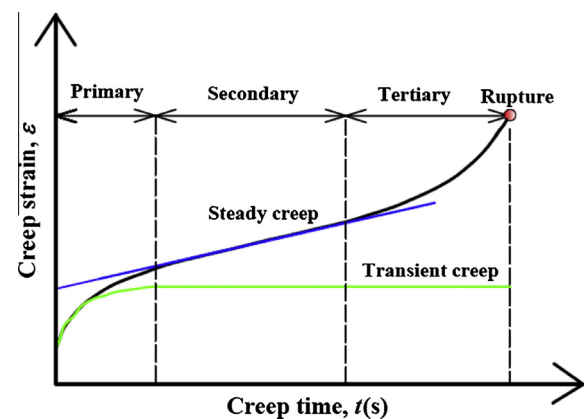


**Fig. 9.** Typical creep curve for viscoelastic materials.



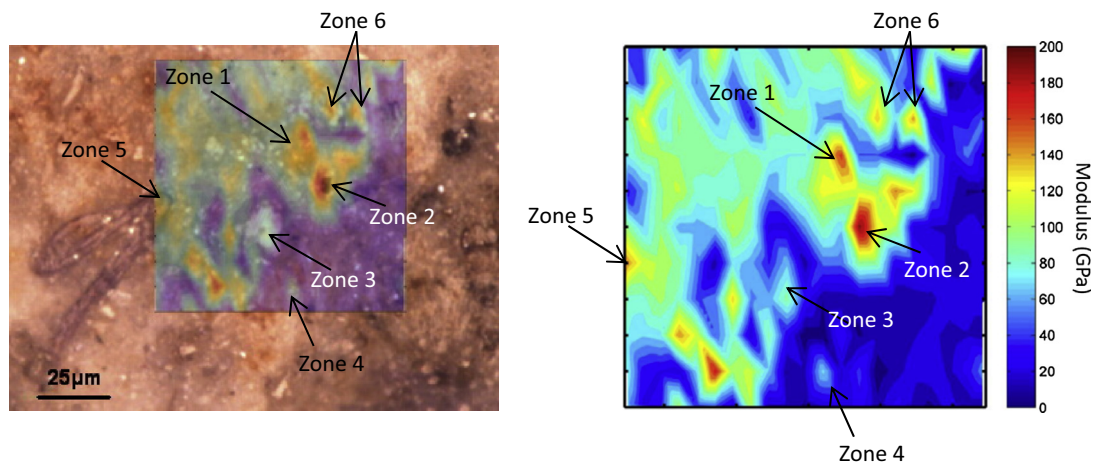


Fig. 10. Contour map of elastic modulus in indent area.

the secondary creep named as steady-state creep as well, during this stage, the creep rate is constant and the plot becomes linear. Steady creep is a crucial stage gives a balance between the competing process of strain hardening and recovery. As for the tertiary

creep stage, grain boundary separation and the formation of internal cracks, cavities, and voids accelerate the rate of creep. During the time-dependent nanoindentation testing, only former two stages can be observed. Therefore, the former two stages can be described as the following equation:

$$h = h_0 - \alpha \cdot e^{-\beta t} + m \cdot t \tag{4}$$

where  $h$  is the holding displacement (nm). The first part of the right-hand side of this equation can be treated as the sudden displacement when the loading is applied. The second part displays the transient deformation. The key feature of transient creep is time constant  $\beta$ , which indicates how long the transient creep lasts. The third part depicts the steady creep, indicating the continuously viscous deformation. The key feature of steady creep is the creep rate  $m$ , which is a constant slope found in displacement varying with time.

Table 6  
Statistical analysis for three regions in indent area.

Item	Red region/GPa	Green region/GPa	Blue region/GPa
Mean value	151.66	91.77	28.05
Range	91.00	76.37	57.70
Standard deviation	27.96	19.26	16.00
Quartile deviation	45.40	38.18	28.86

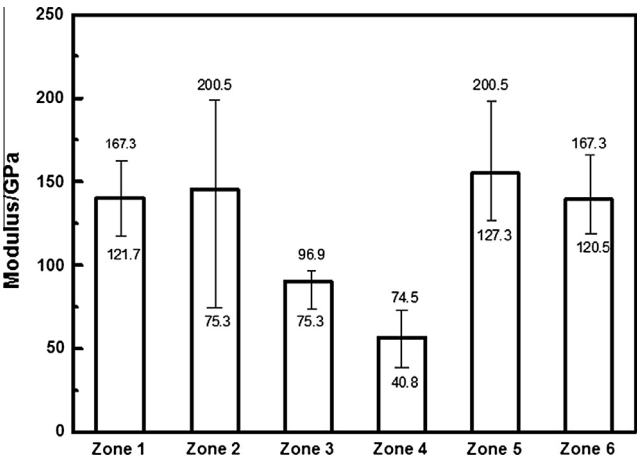


Fig. 11. Elastic modulus in six zones (minimum, maximum, and mean values of elastic modulus have been marked).

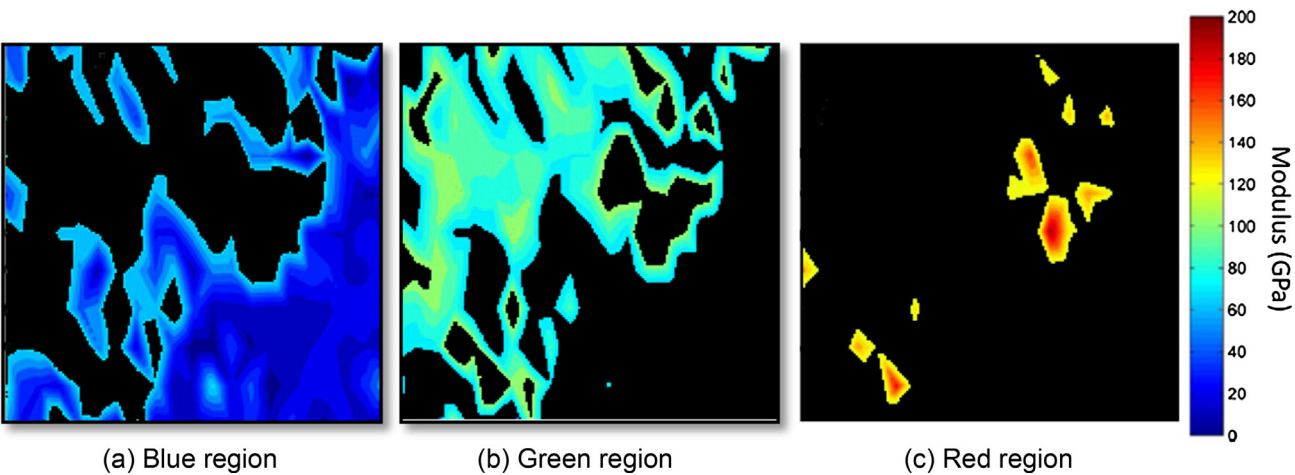


Fig. 12. Different modulus region extracted based on the image processing technique.



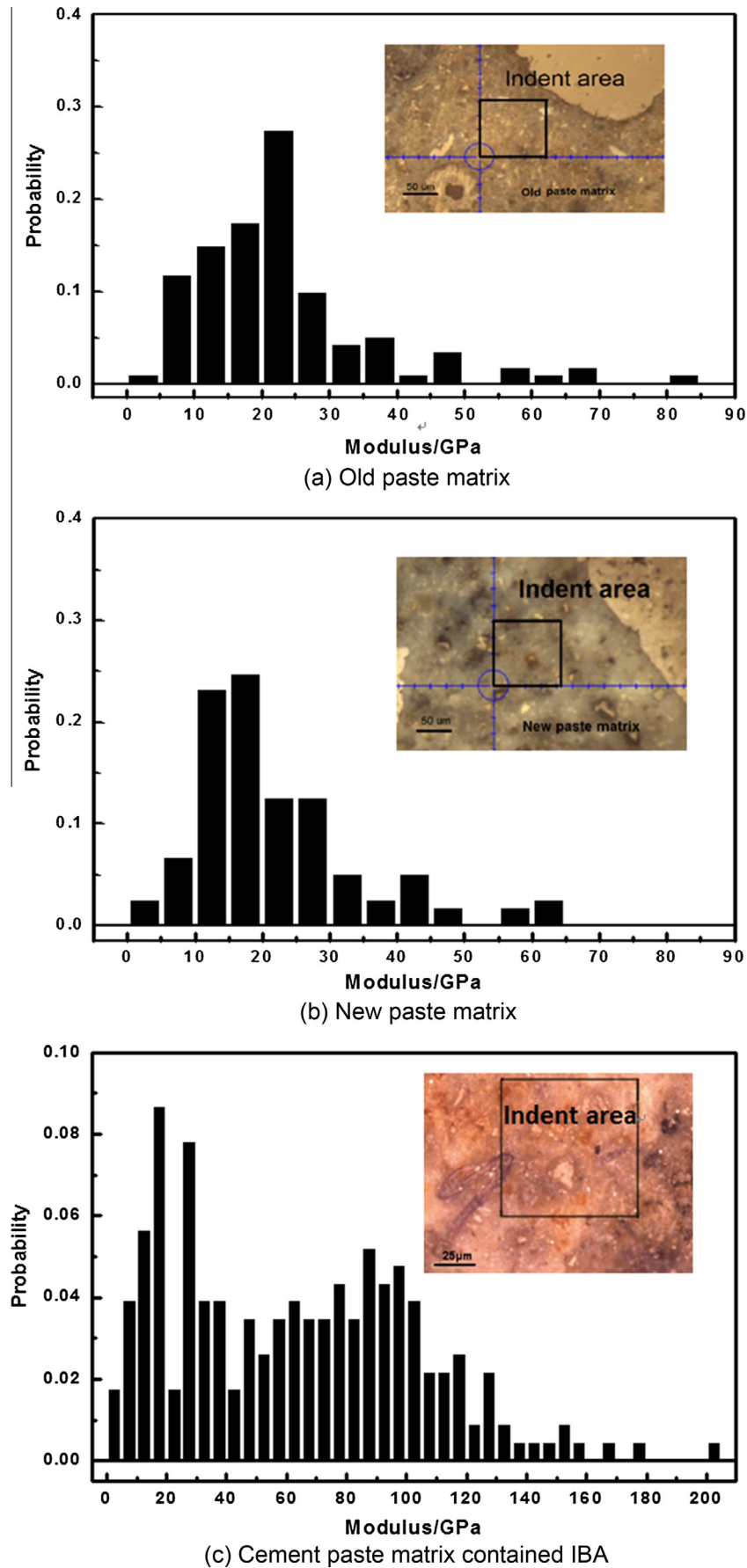


Fig. 13. Modulus probability in indent area (the data in (a) and (b) from Ref. [41]).

## 2.4. Microstructure from FESEM testing

Generally, field-emission scanning electron microscopy (FESEM) can get the microscopy information concerning surface crystallography, surface morphology, and surface composition. Here, high-resolution FESEM was used to study the microstructure of cement mortar contained IBA. As we more cared about the morphologic properties, the Scatter Electron Images were collected under 15 kV accelerating voltage.

## 2.5. Chemical identification

Elemental investigation of the NI sample was carried out by Energy-dispersive X-ray (EDX) Spectrometer attached to an FESEM. Phase maps with elemental distribution and associated spectra were generated. Approximately a 100  $\mu\text{m}$  square selected area was analyzed, which may enable the assessment of correlation between the nanoindentation mechanical results and the components of the IBA involved.

## 3. Results and discussion

### 3.1. Nano-scale mechanical properties

#### 3.1.1. Elastic modulus

Based on the records of loading-unloading curves of 231 indentations, elastic modulus for each indent point was calculated according to Eq. (1). Then, the situ 2D mapping of elastic modulus in indent area is presented as shown in Fig. 10. It is obviously observed that because of the components diversity in IBA mixtures, the elastic modulus in different region presents apparent variability. Six zones marked in indent area indicate six different substances (different substances will be displayed visually in different color from Optical microscope observation, see Fig. 10), thereby their chemical compositions are also quite different, leading to a large difference in mechanical properties. For example, the smallest elastic modulus in indent area is 1.5 GPa (in blue color region), while the largest elastic modulus is around 200 GPa (found in Zone 2).

Besides, the elastic moduli in six zones are rather different, see Fig. 11. The minimum, maximum, and mean values of elastic modulus in the interested zones were marked in Fig. 11 also. The macroscopic mechanical characteristic of the concrete material is integrated exhibition of the inner mechanical characteristic of this kind of material in nanoscopic view. Especially for the cement concrete contained IBA, the inner heterogeneity is important to its macroscopic crack form. When force is evenly distributed over its area, however, because of the nano-scale heterogeneity of materials, a non-uniform stress field will be occurred, even probably producing a localized increase in stress, resulting in the stress concentration phenomenon. Actually, fatigue cracks always start at stress concentrated area. From Fig. 11, it is observed that six zones have quite different elastic modulus range. Especially, in Zone 4, the elastic modulus varies from 40.8 GPa to 74.5 GPa, while in Zone 2, the elastic modulus changes from 75.3 GPa to 200.5 GPa. Therefore, the inhomogeneity phenomenon is quite distinct.

To further illustrate the materials' heterogeneity, statistical analysis method is used. Based on the image processing technique, the indent area is separated into three regions for partition statistic, namely, blue region, green region, and red region as shown in Fig. 12. The indices used to quantify the amount of variation or dispersion of a set of data values, such as standard deviation and quartile deviation were calculated for these three regions, as listed in Table 6. The mean value of elastic modulus in red region is almost 5 times larger than the value in blue region. However, the standard

deviation in blue region is much smaller. It can be concluded that the blue region has a relatively homogeneous mechanical property, and the green region takes second place, while the red region has a relatively heterogeneous mechanical characteristic.

Histograms of modulus distribution frequency were plotted in Fig. 13. To compared with the conventional recycled aggregate cement mortar, the analyze indentation data were collected from Ref. [35] for old and new paste matrix. The water-cement ratio (w/c) used in Ref. [35] is 0.45, smaller than w/c we used, since IBA is a porous material with higher water absorption capability. From Fig. 13, it can be found out that the moduli in old paste matrix vary from 3.8–85 GPa, in new paste matrix vary from 2–64 GPa, while in our tested matrix, the moduli vary from 1.5–200 GPa. The probable reason is that the contaminants such as mental increase the modulus in the indent area, while the other kind of contaminants such as ceramic and the brick lower the modulus. Based on the data collected from Fig. 13, Table 7 gives the mean values, range, quartile deviation, and coefficient of variation of three indent areas. Obviously, the mean modulus of the cement mortar contained IBA is much larger than the cement mortar contained recycled aggregate. However, this doesn't indicate that the IBA cement mortar has a stiffer mechanical behavior. Judged from the range, quartile deviation, and coefficient of variation, IBA cement mortar has much higher values, means that this kind of

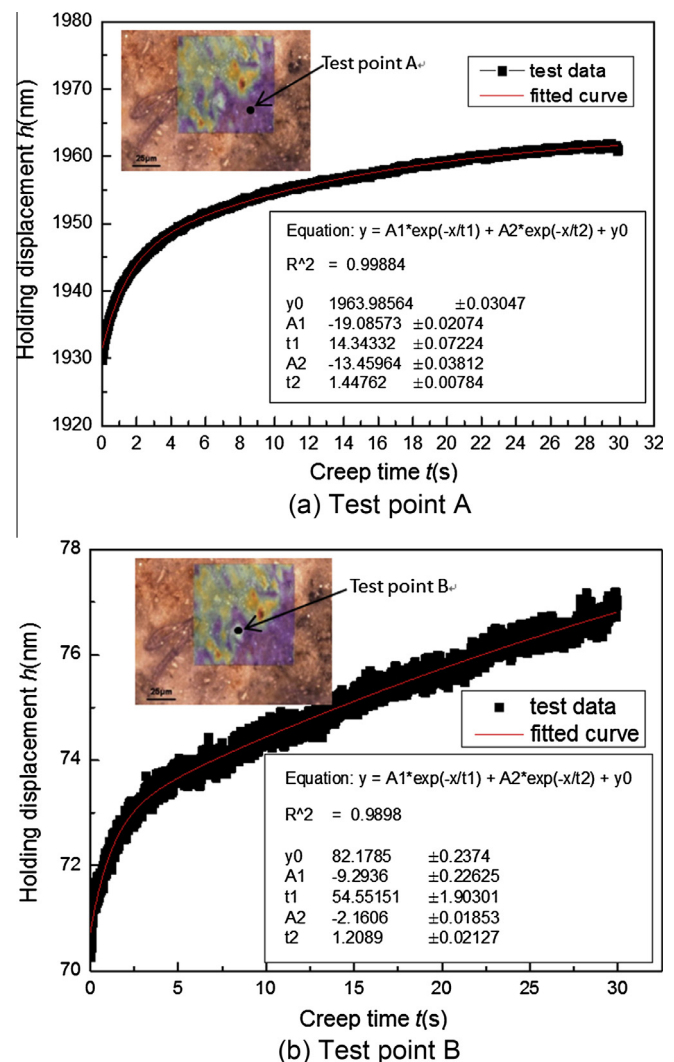


Fig. 14. Creep time-holding displacement curves for two test points.

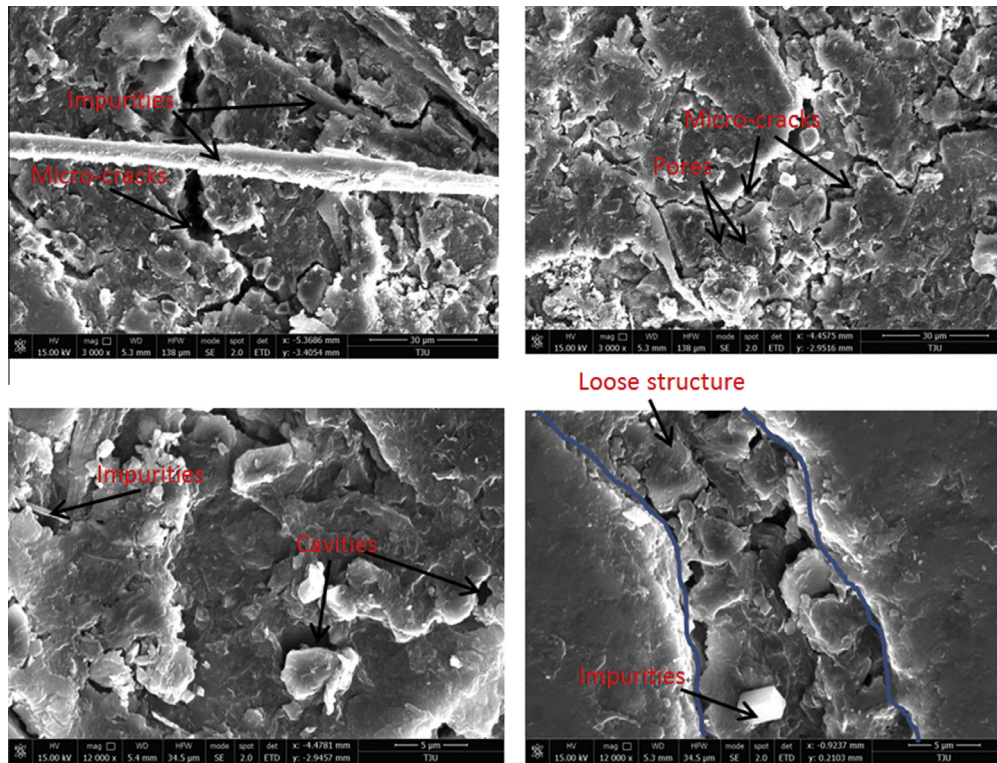


Fig. 15. SE images of cement mortar containing IBA.

cement composite presents apparent materials' heterogeneity. And this kind of materials' heterogeneity is highly possible resulting in the non-uniform stress distribution, making it difficult to predict its failure mode accurately.

### 3.1.2. Creep behavior

Two test points were selected (as marked in Fig. 14) to proceed time-dependent nanoindentation testing. One test point randomly selected was located in blue region since this region seems much softer than the other two regions, which may present more apparent creep characteristic. The other one was located in Zone 3, which has much higher stiffness. Based on the loading behavior illustrated in Fig. 8, the creep time  $t(s)$ -holding displacement  $h$  (nm) curves can be derived, see Fig. 14. Apparently, under the influence of mechanical stresses, Test point A deforms much more quickly than Test point B. After 30 s exposure to high levels of stress, the total deformation value at Point A is almost 25 times larger than that at Point B. Fitted by the second-order exponential decay function,

$$h(t) = y_0 + A_1 e^{-\frac{x}{t_1}} + A_2 e^{-\frac{x}{t_2}} \quad (5)$$

the parameters  $y_0$ ,  $A_1$ ,  $A_2$ ,  $t_1$ ,  $t_2$  can be figured out. Then, the parameters describing the key features of transient creep and steady creep were easily obtained according to Eq. (4).

The parameters calculated from Eq. (5) are listed in Table 8. Observed from above two figures, the holding displacement progressively increases up to about  $5\beta^{-1}$  time after the start of the experiment. Then, a quasi-constant displacement increase rate can be found over the whole important part of the total creep time. It is obviously that the viscoelastic time constant value  $\beta^{-1}$  and the creep rate value  $m$  at test point B are all smaller than the values at point A. It indicates that point A is much more creepy compared to the point B, which has a steady creep rate of around 0.1 nm/s. Since the cement mortars contained IBA are a class of complex chemo-mechanical materials that possess a high degree of heterogeneity,

the creep heterogeneity among the constituents at micro-scale is inevitable. The creep damage is still a major failure mode for concrete during the service life, however, because of the complex multiscale heterogeneity, the crack-initiating and crack-propagating mechanisms are rather difficult to predict and identify.

### 3.2. Microstructural observation

The microstructures of different test regions were analyzed based on Secondary Electron (SE) photographs as presented in Fig. 15. Many pores, cavities, micro-cracks, impurities, and loose structures can be found. Due to a large amount of impurities (glass, brick, ceramics, metal, etc.) are embedded into the cement mortar, fine particles fail to bridge the gaps between the matrix and aggregates, a continuous, smooth, and uniform connection between matrix and aggregates are cut off, resulting in the formation of microcracks, pores, and cavities. Therefore, the microstructure of the blended cement paste containing IBA is less uniform and

Table 7

Statistical analysis for cement mortar contained recycled aggregate and IBA aggregate.

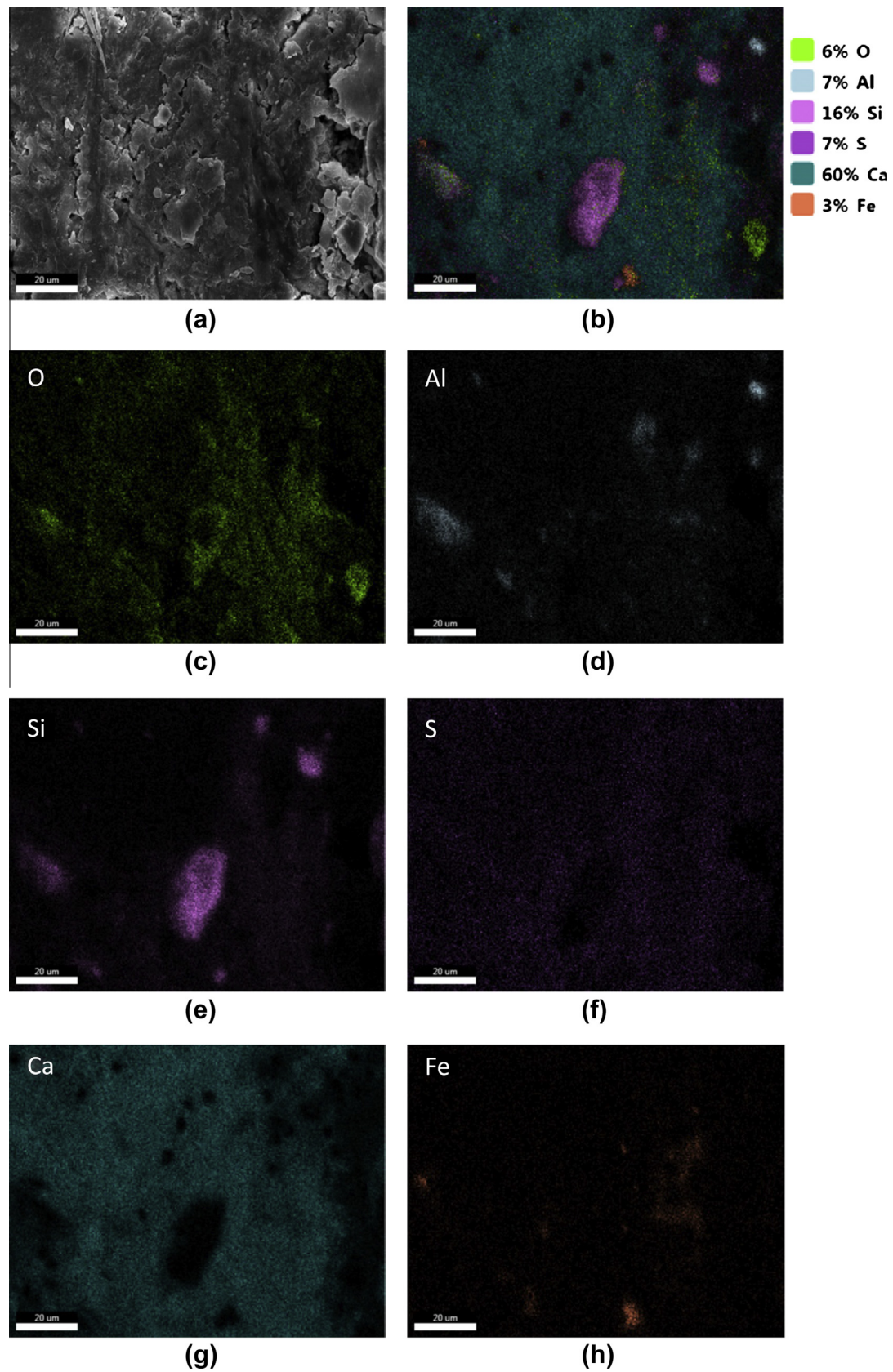
Item	Fig. 13(a)	Fig. 13(b)	Fig. 13(c)
Mean(MPa)	23.04	21.92	63.24
Range(MPa)	80	60	200
Quartile deviation(MPa)	40	30	100
Coefficient of variation	59.31%	57.25%	64.05%

Table 8

Time constant and creep rate for testing points A and B.

Item	Test point A	Test point B
$\beta^{-1}$	2.78 s	1.68 s
$m$	0.36 nm/s	0.12 nm/s





**Fig. 16.** EDX compositional mapping in ROI: (a) FESEM image for testing region; (b) superposition of all interested six elements; (c)~(h) are elemental spatial distribution images for oxygen (O), aluminum (Al), silicon (Si), sulfur (S), calcium (Ca), and iron (Fe), respectively.



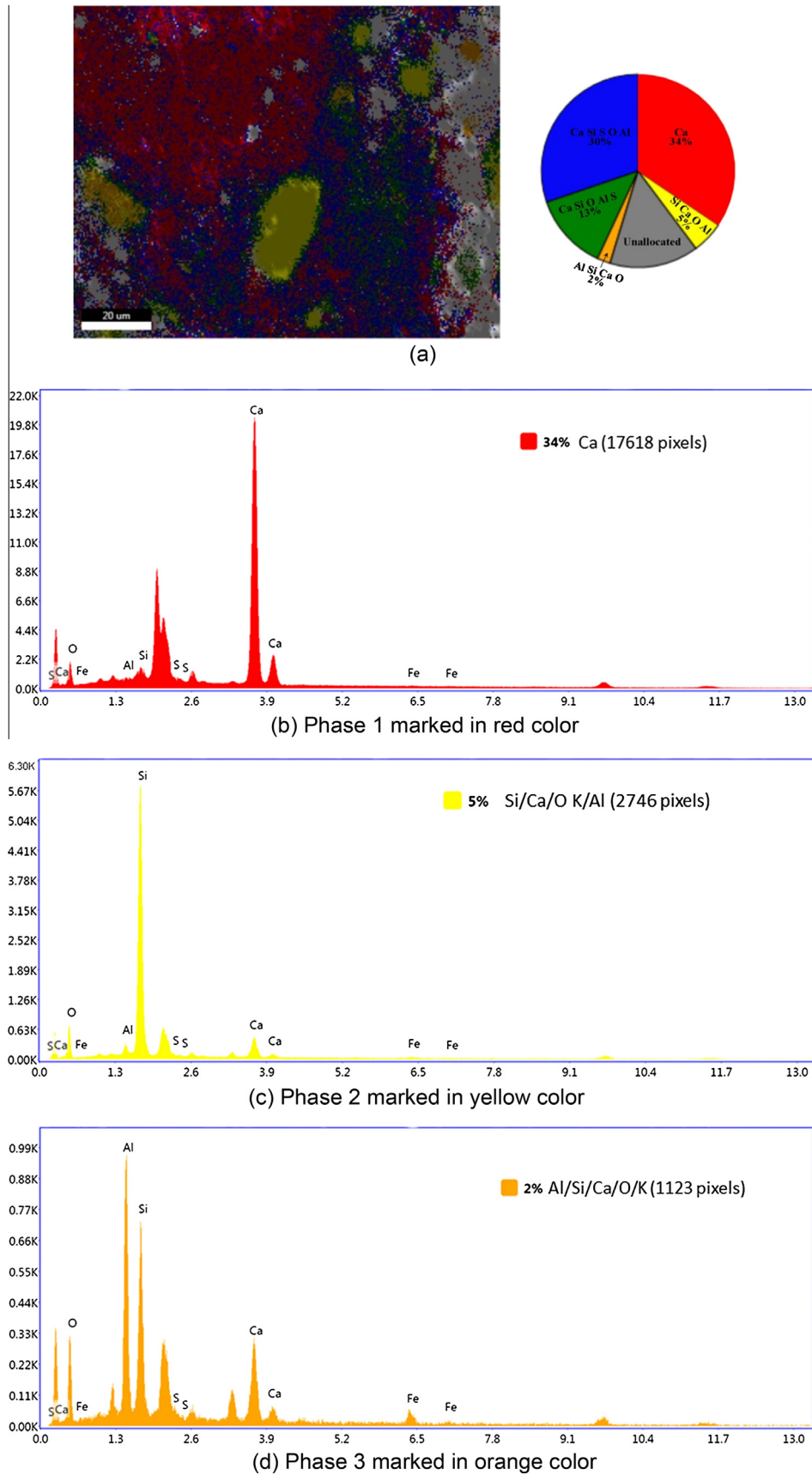


Fig. 17. Phase maps and X-ray microanalysis-EDX of test regions.

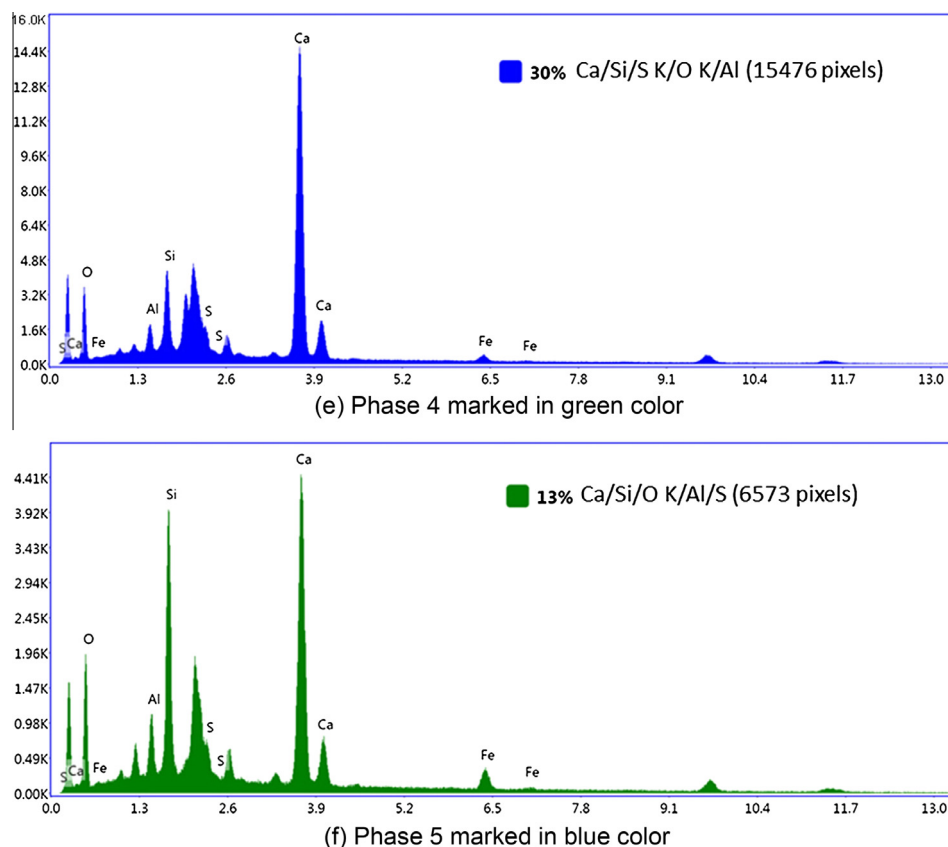


Fig. 17 (continued)

compact. From above observation, it can be confirmed that the components heterogeneity leads to the intrinsic microstructural non-uniform, which may further forms a highly inhomogeneous mechanical response at the nano-level.

### 3.3. Chemical investigation

The field-emission scanning electron micrograph (Fig. 16(a)) and corresponding EDX elemental analyses were acquired. Principal elements as listed in Table 3 were captured, including oxygen (O), calcium (Ca), silicon (Si), aluminum (Al), iron (Fe), and sulfur (S). The size of region of interest (ROI) is  $126 \times 100 \mu\text{m}$ . The spatial distribution of above six principal elements is mapped in different color, see Fig. 16(b)–(h). The order of  $\text{Ca} > \text{Si} > \text{Al} > \text{S} > \text{O} > \text{Fe}$  for their occurrence in the testing region is observed. A More homogeneous Calcium, Oxygen, and Sulfur distribution is observed on the test region. Especially, the Ca ions alongside the phase map take up 60% pixels of the whole region. It is quite reasonable since calcium is easy to be found in a broad variety of species including portlandite, lime, calcite, hydrocalumite phases that are highly possible produced during the course of incineration. Besides, elevated concentration of sulfur ions is another outstanding feature of IBA embedded cement mortar, see Table 3. The existing Fe-rich phases are also found, indicating the concentrations of Fe-bearing minerals particularly in the margins.

After tens of minutes' data acquisition, the phase mapping routine supported by the TEAM™ software automatically separated and color coded the difference phases of the test sample as shown in Fig. 17(a), in which 15% pixels were unallocated. Phase spectrums from the pixels for each individual phase were generated, see Fig. 17(b)–(f). Here five phases were focused. By comparing the measured spectra to a group of phase spectra of main

components of IBA, finding discrepancies and similarities between spectra, the potential substances of distinct stoichiometry can be roughly identified. For example, the red and blue phases occupy the majority region of the tested area (34% and 30% of the total area, respectively), and they have quite similar phase spectra. Slag is considered having the same activity as cementitious materials, when reacting with water, hydration rim will be formed around the slag particles. Actually, hydration products of slag are principally the same as that of ordinary Portland cement [37]. However, when the slag is blended with the Portland cement, the stoichiometry results are more complicated, i.e., the atomic ratio Ca/Si in bulk calcium silicate hydrate gel (C-S-H) is reduced due to the clinker hydration, the formation of hydrotalcite partially accommodated of MgO and  $\text{Al}_2\text{O}_3$  within the C-S-H phase occurs, Mg enters a hydrotalcite-type phase while some of  $\text{Al}_2\text{O}_3$  enters an Afm phase along with the  $\text{S}^{2-}$  released from the slag, meanwhile Katoite may also formed as the slag product. By comparison with above phenomenon, the red and blue regions are more likely the slag cement-hydrate products. Except for the slag as a main component, glass, brick, ceramics and metal also may contain in the test regions. Since the elements Si and O take up 47.17% and 29.51% by weight, respectively, the yellow phases dominated by the silicon/aluminum/calcium intensity regions can be identified as glass-bearing areas ( $\text{SiO}_2$  is its main composition). Based on the XRD test results, quartz ( $\text{SiO}_2$ ), Mullite ( $\text{Al}_{2.8}\text{Si}_{1.2}\text{O}_{9.54}$ ), Osbornite ( $\text{TiN}$ ), and Loveringite ( $\text{CaTi}_2\text{O}_{38}$ ) are the major phases existed in the ceramic. Therefore, by contrast with the measured spectra, the orange regions can probably be represented by the ceramic-bearing areas.

Cementitious materials have been recognized as multi-scaled materials, with a strong heterogeneity that manifests itself at multiple scales. Such complexity is further increased by the use

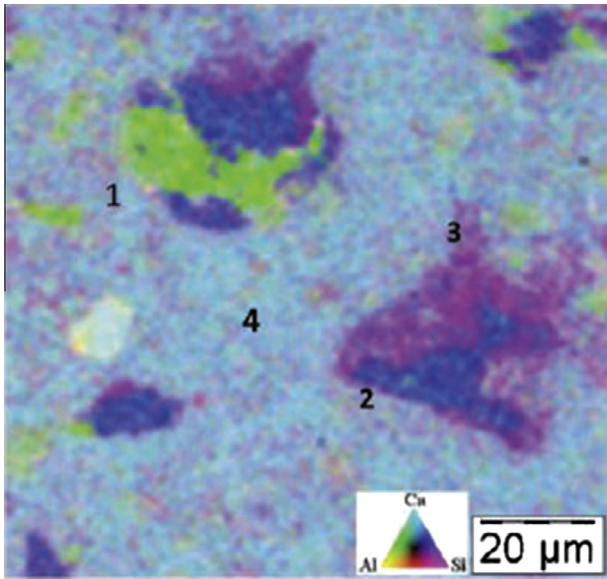


Fig. 18. SEM-EDS map for conventional cement mortar in Ref. [38].

of bottom ash aggregates in cements, multiple impurities and active components lead to the formation of multiple pore spaces, micro-cracks, and new generated nano-phases. By contrast, the SEM-EDS map for the pure cement mortar using a w/b ratio of 0.36 is presented in Fig. 18. C4AF clinker phases (Tetra-calcium Aluminoferriite, label 1, green phase), C3S clinker phase (Tricalcium Silicate, label 2, blue phase), HD CSH (High-density CSH, label 3, violet blue phase), and LD CSH (Low-density CSH, label 4, violet blue phase) can be clearly identified. Compared with the phase map in Fig. 17(a), for IBA cement mortar, the chemical compositions are more complicated and hardly can be identified properly just through EDX, resulting in a more distinct chemical heterogeneous than the conventional cement composites. Since the local mechanical properties are always determined by the material chemistry, above micro-scale chemical heterogeneity observed from FESEM-EDX results may explain the experimental variability and non-linearity of IBA cement composites.

#### 4. Conclusions

This work constitutes an original Nanometrology technique to the problem of heterogeneity characterization for IBA cement mortar from the point of view of chemistry, microstructure, and micromechanics. It is shown that the combination of the newly developed nanoindentation mechanical measurement (elastic and viscoelastic behavior) together with FESEM morphology observation and EDX phase/elemental mapping provides a sufficient base of observables to identify why the heterogeneity will happen and how the heterogeneity will affect the mechanical behavior of the mixtures. The main conclusions can be drawn as follows:

- 1) Because of the components diversity in IBA mixtures, the nanoindentation elastic modulus and creep parameters in different region present apparent variability. Compared with the conventional recycled aggregate cement mortar, IBA cement mortar presents more apparent materials' inhomogeneity and mechanics' heterogeneity.
- 2) It is seem that nanoindentation testing together with the image processing technique and statistical analysis is probably a good methodology to give a quantitative evaluation of the degree of mechanical heterogeneity in target test regions at nano-scale.

- 3) Based on the FESEM observation, it can be confirmed that the components heterogeneity leads to the intrinsic microstructural non-uniform. Due to a large amount of impurities are embedded into the cement mortar, fine particles fail to bridge the gaps between the matrix and aggregates, more pores, cavities, micro-cracks, and loose structures will be generated.
- 4) Based on the chemical investigation, it is found that hydration products of slag are principally the same as that of ordinary Portland cement. However, when the slag is blended with the Portland cement, the stoichiometry results are more complicated, some new nano-phase will be produced and some major atomic ratio will be re-balanced. In addition to this, other impurities (such as glass, brick, ceramics, metal, etc.) are randomly distributed in the samples, leading to the formation of multiple pore spaces, micro-cracks, and new generated nano-phases. All above make the chemical compositions of IBA cement mortar are more complicated and hardly can be identified properly just through EDX, resulting in a more distinct chemical heterogeneous than the conventional cement composites.

This paper has made a significant contribution to the use of nanoindentation for testing mixtures contained IBA. It is evident from this study that nanoindentation can provide micromechanical property of different constitute of mixtures. Consequently, the property from nanoindentation test may provide more precise input data for the micromechanical numerical models for characterizing damage behavior of mixtures contained IBA. Besides, the study on heterogeneity of mixtures contained IBA is of practical significance in the project application of IBA and production process of IBA. Nanoindentation elastic/creep testing, FESEM observation, and EDX chemical analysis give mutual verification to illustrate the heterogeneous phenomenon in IBA cement mixtures, which give the reason for the variation of mixtures' macro properties. The result is particularly useful for guiding mix designing. Meanwhile, the result highlights the need for improving production technology of IBA to guarantee its uniformity, such as removing constituents with quiet high or low elastic modulus. Despite all this potential application, there is some limitation in this study that a quantitative relation among micromechanical, microstructural, and chemical parameters to identify the degree of heterogeneity is still unknown, which will be discussed in our future research.

#### Acknowledgement

The work described in this paper is supported by the Innovation Program of Shanghai Municipal Education Commission (No. 15ZZ017), National Natural Science Foundation of China (Nos. 11102104, U1433201), and Program for Young Excellent Talents in Tongji University.

#### References

- [1] A. Poletini, R. Pomi, E. Fortuna, Chemical activation in view of MSWI bottom ash recycling in cement-based systems, *J. Hazard. Mater.* 162 (2009) 1292–1299.
- [2] O. Hjelm, J. Holm, K. Crillesen, Utilisation of MSWI bottom ash as sub-base in road construction: first results from a large-scale test site, *J. Hazard. Mater.* 139 (2007) 471–480.
- [3] A. Demirbas, Waste management, waste resource facilities and waste conversion processes, *Energy Convers. Manage.* 52 (2011) 1280–1287.
- [4] Rafat. Siddique, Utilization of municipal solid waste (MSW) ash in cement and mortar, *Resour. Conserv. Recycl.* 54 (2010) 1037–1047.
- [5] J. Nader Ghafoori, Bucholtz, Investigation of lignite-based bottom ash for structural concrete, *J. Mater. Civil. Eng.* 8 (1996) 128–137.
- [6] J. Sanjeev Kumar, Stewart, Evaluation of Illinois pulverized coal combustion dry bottom ash for use in geotechnical engineering applications, *J. Energy Eng.* 129 (2003).

- [7] L.B. Andrade, J.C. Rocha, M. Cheriaf, Evaluation of concrete incorporating bottom ash as a natural aggregates replacement, *Waste Manage.* 27 (2007) 1190–1199.
- [8] O. Gines, J.M. Chimenos, A. Vizcarro, J. Formosa, J.R. Rosell, Combined use of MSWI bottom ash and fly ash as aggregate in concrete formulation: environmental and mechanical considerations, *J. Hazard. Mater.* 169 (2009) 643–650.
- [9] M. Izquierdo, X. Querol, A. Josa, E. Vazquez, A. Lopez-Soler, Comparison between laboratory and field leachability of MSWI bottom ash as a road material, *Sci. Total Environ.* 389 (2008) 10–19.
- [10] R. Del Valle-Zermeno, J.M. Chimenos, J. Giro-Paloma, J. Formosa, Use of weathered and fresh bottom ash mix layers as a subbase in road constructions: environmental behavior enhancement by means of a retaining barrier, *Chemosphere* 117 (2014) 402–409.
- [11] M.M. Abdulahi, Municipal solid waste incineration bottom ash as road construction material, *AU J.T.* 13 (2009) 121–128.
- [12] I. Maria, V. Enric, Q. Xavier, B. Marilda, L. Àngel, P. Felicià, Use of bottom ash from municipal solid waste incineration as a road material, *International Ash Utilization Symposium*, University of Kentucky, 2001.
- [13] M.M.T. Eymae, W.D. Wijs, D. Mahadew, The use of MSWI bottom ash in asphalt concrete, *Stud. Environ. Sci.* 60 (1994) 851–862.
- [14] T.C. Lee, Z.S. Li, Conditioned MSWI ash-slag-mix as a replacement for cement in cement mortar, *Constr. Build. Mater.* 24 (2010) 970–979.
- [15] Y.T. Kim, C. Lee, H.I. Park, Experimental study on engineering characteristics of composite geomaterial for recycling dredged soil and bottom ash, *Mar. Georesour. Geotechnol.* 29 (2011) 1–15.
- [16] Y.T. Kim, T.H. Do, Effect of bottom ash particle size on strength development in composite geomaterial, *Eng. Geol.* 139–140 (2012) 85–91.
- [17] R. Forteza, M. Far, C. Segui, V. Cerda, Characterization of bottom ash in municipal solid waste incinerators for its use in road base, *Waste Manage.* 24 (2004) 899–909.
- [18] E. Toraldo, S. Saponaro, A. Careghini, E. Mariani, Use of stabilized bottom ash for bound layers of road pavements, *J. Environ. Manage.* 121 (2013) 117–123.
- [19] S.C. Blair, N.G.W. Cook, Analysis of compressive fracture in rock using statistical techniques: part i. a non-linear rule-based model, *J. Rock. Mech. Min. Sci.* 35 (1998) 837–848.
- [20] J.M. Chimenos, M. Segarra, M.A. Fernandez, F. Espiell, Characterization of the bottom ash in municipal solid waste incinerator, *J. Hazard. Mater.* 64 (1999) 211–222.
- [21] J.M. Chimenos, A.I. Fernandez, L. Miralles, J.R. Rosell, A.N. Ezquerro, Change of mechanical properties during short-term natural weathering of MSWI bottom ash, *Environ. Sci. Technol.* 39 (2005) 7725–7730.
- [22] J. Carmeliet, R.D. Borst, Stochastic approaches for damage evolution in standard and non-standard continua, *Int. J. Solids Struct.* 32 (1994) 1149–1160.
- [23] C.A. Tang, S.Q. Kou, Crack propagation and coalescence in brittle materials under compression, *Eng. Fract. Mech.* 61 (1998) 311–324.
- [24] H. Wang, J. Wang, J. Chen, Micromechanical analysis of asphalt mixture fracture with adhesive and cohesive failure, *Eng. Fract. Mech.* 132 (2014) 104–119.
- [25] Lei Zhang, Wenwei Wang, Kent A. Harries, Jun Tian, Bonding behavior of wet-bonded GFRP-to-concrete interface, *J. Compos. Constr.* 19 (2015).
- [26] X. Yu, M. Zaumanis, S. dos Santos, L.D. Poulikakos, Rheological, microscopic, and chemical characterization of the rejuvenating effect on asphalt binders, *Fuel* 135 (2014) 162–171.
- [27] G.C. Lee, H.B. Choi, Study on interfacial transition zone properties of recycled aggregate by micro-hardness test, *Constr. Build. Mater.* 40 (2013) 455–460.
- [28] Andreas Jäger, R. Lackner, Identification of viscoelastic model parameters by means of cyclic nanoindentation testing, *Int. J. Mater. Res.* (2008) 1–7.
- [29] K.J. Krakowiak, W. Wilson, S. James, S. Musso, F.J. Ulm, Inference of the phase-to-mechanical property link via coupled X-ray spectrometry and indentation analysis: application to cement-based materials, *Cem. Concr. Res.* 67 (2015) 271–285.
- [30] S.Y. Chang, H.-C. Tsai, J.Y. Chang, S.J. Lin, Y.S. Chang, Analyses of interface adhesion between porous SiOCH low-k film and SiCN layers by nanoindentation and nanoscratch tests, *Thin Solid Films* 516 (2008) 5334–5338.
- [31] M. Miller, C. Bobko, M. Vandamme, F.-J. Ulm, Surface roughness criteria for cement paste nanoindentation, *Cem. Concr. Res.* 38 (2008) 467–476.
- [32] C. Hu, Z. Li, A review on the mechanical properties of cement-based materials measured by nanoindentation, *Constr. Build. Mater.* 90 (2015) 80–90.
- [33] X. Yuetao, J.C. David, J. Feng, Z. Hu, P.S. Surendra, Experimental study of the interfacial transition zone (ITZ) of model rock-filled concrete (RFC), *Cem. Concr. Compos.* 55 (2015) 223–231.
- [34] R.D. Moser, P.G. Allison, M.Q. Chandler, Characterization of impact damage in ultra-high performance concrete using spatially correlated nanoindentation/SEM/EDX, *J. Mater. Eng. Perform.* 22 (12) (2013) 3902–3908.
- [35] X. Jianzhuang, L. Wengui, S. Zhihui, A.L. David, P.S. Surendra, Properties of interfacial transition zones in recycled aggregate concrete tested by nanoindentation, *Cem. Concr. Compos.* 37 (2013) 276–292.
- [36] L. Wengui, X. Jianzhuang, S. Zhihui, K. Shiho, P.S. Surendra, Interfacial transition zones in recycled aggregate concrete with different mixing approaches, *Constr. Build. Mater.* 35 (2012) 1045–1055.
- [37] H.F.W. Taylor, *Cement Chemistry*, Thomas Telford, London U.K, 1997.
- [38] M. Sebastiani, Mapping the Mechanical Properties of Cement-based Materials By Using CSM and Ultra-fast Nanoindentation. <<http://cp.literature.agilent.com/litweb/pdf/5991-3389EN.pdf>> 2012 (accessed 16.02.07).